https://sjdfs.journals.ekb.eg/

Magneto-Electric Influence on a Functionally Graded Porous Hollow Structure in Hygrothermal Environment

R. Tantawy [1*]

[1]Department of Mathematics, Faculty of Science, Damietta University, Damietta 34517, Egypt.

Abstract

The influence of porosity and magnetic field on a mathematical model of functionally graded piezoelectric (FGP) hollow structures (cylinder and sphere) in a hygrothermal environment is presented using a semi-analytical technique. The mathematical model is under the effects of many forces, in addition to a magnetic field, which is still a challenging study. Loading is a collection of mechanical pressure on the inner and outer surface, magnetic field, hygrothermal influences, and change of electric potentials between external and internal surfaces. The whole material properties are supposed to be a polynomial function of radius. Numerical results discuss four different boundary conditions for each model of mechanical pressure and electric field subject to the influence of temperature, humidity, and magnetic field. To check the numerical results, the results are compared between functionally graded porous and non-porous hollow structures. In the end, numerical outcomes clarified the influence of the porosity factor in the mathematical models and its importance in mechanical engineering and modern technology.

Keywords: Porous material; Functionally graded material; Hygrothermal influence; Semi-analytical technique; Piezoelectric effect; Magnetic field.

Introduction

A porous environment or a porous material is a substance containing holes. A porous material is described by porosity. Other properties of the medium (permeability, resistance, electric conductivity) can be obtained from the attributes of its constituents. A lot of natural materials such as rocks and soil (petroleum, aquifers), biological tissues (wood, bones), and manufactured materials (ceramics, cement) can be treated as porous materials. A lot of their properties can only be explained by considering them to be porous materials. The hypothesis of porous material is applied in many fields of applied science and mechanical engineering. Porous functionally graded materials are porous structures with porosity gradients distributed over volume (Zhang and Wang, 2017). They have many uses in shipbuilding, the science of biomedical, dental medical implants, the aerospace industry, and other industries. For

porous functionally graded material and their relationship with moisture and temperature, Tahir *et al.* (2021) investigated wave propagation of porous FG sandwich plate in a hygrothermal environment, six different porosity models are studied to show the porosities distribution operator. She *et al.* (2019) used the nonlocal strain gradient theory in the wave propagation of nanotubes to clarify the influences of porosities and hygro-thermal changes. Singh and Harsha (2021) used the sigmoid function to study the porosity effect on vibration and buckling for sandwich plates reinforced with various boundary conditions at the edges. The solution technique was applied for six of 21 boundary conditions. A refined quasi-3D shear deformation theory for bending, buckling and free vibration analyses of FG porous beam with two different porosity distributions resting on an elastic foundation is studied by Fahsi *et al.* (2019). Penna *et al.* (2021) presented the bending response of FG porous Bernoulli-Euler nano-beams under hygro-thermo-mechanical force. Nikrad *et al.* (2021) displayed FG porous curved beams with different cases of porosity by using the first-order shear deformation theory with the nonlinear Green strains. Moreover, a lot of researchers discuss the porosity properties of functionally graded materials.

Different articles about piezoelectric porous functionally graded shapes are studied. Jankowski *et al.* (2021) explained piezoelectric loading on bifurcation buckling of porous FGM nanobeam based on a higher-order nonlocal elasticity and strain gradient theory in coincidence with Reddy's third-order shear deformation beam theory. Zhao *et al.* (2020) used Euler-Bernoulli beam and strain gradient theories to explore the bending and vibration of FG porous flexoelectric nanobeam. Alghanmi and Zenkour (2021) display the analysis of static bending of porous FG sheets joined to a piezoelectric fiber-reinforced composite layer. The sheet is exposed to sinusoidal mechanical and electrical force. Ghobadi *et al.* (2021) used the modified flexoelectric theory to study the effect of porosity on the diverse distribution of the static and nonlinear dynamic responses of a sandwich FG nanostructure with thermo-electro-elastic coupling. Tantawy and Zenkour (2022) presented the hygrothermal influence on FGP hollow porous spheres with the effect of mechanical and electrical loading.

Several types of research are still concerned

with the piezoelectric functionally graded material and different loading on it. Allam *et al.* (2018) obtained a semi-analytical technique for an exponentially graded piezoelectric hollow sphere. The loading on a sphere is electric potentials, electric displacement, magneto-thermo-elasticity, and hygrothermal effect to explain the specific effects of the material gradation in modern technology. Arefi and Zenkour (2017) used Eringen's nonlocal theory with piezomagnetic layers affected by electric and magnetic potentials resting on a two-parameter foundation to study. Further research papers are created for functionally graded materials, such as Refs. (Zenkour and Aljadani, 2020; Sobhy and Zenkour, 2019; Zenkour and Alghanmi, 2021; Allam *et al.*, 2016; Dai *et al.*, 2012; Arani *et al.*, 2012) to clarify the effect of FGMs on some particular applications.

This paper is interested in the magneto hygrothermal actions on porous functionally graded piezoelectric hollow structures (cylinder and sphere). The material characteristic for porous hollow structures are varying through the radius thickness by the power functions formula. The mechanical boundary conditions on the porous structures are subjected to various sets of internal and external pressures. The differential equations are solved in general by using a semi-analytical technique to obtain the complete solution of the model. Several effective cases are studied to illustrate the effect and importance of the porosity factor and magnetic field on a functionally graded hollow structure in a hygrothermal environment. The results are collected for future studies and comparing the results for stresses, displacement, and electric potential between perfect FGPM and porous FGPM. Finally, the influence of various boundary conditions for four sets in every structure is verified.

Mathematical description of porous hollow FGP structures

This paper pursues to illustrate the effect of a combination of hygrothermal distribution and mechanical loading on a porous FG boundless long and axisymmetric hollow cylinder and symmetric a porous FG hollow sphere. Consider the hollow structures have perfect conductivity and are placed in a stable magnetic field. The geometry of the model is cylindrical coordinates (r, θ, z) and spherical coordinates

(r, θ, φ). The porous (FGP) hollow structures are composed of PZT-4 on the inner surface and Cadmium selenide on the outer one. Table 1 presented the material properties of the model.

Table 1. Mechanical and electrical constants for PZT-4 and Cadmium selenide.

PZT-4	Cadmium selenide
$c_{rr}^{(a)} = 115 \times 10^9$ (Pa)	$c_{rr}^{(b)} = 83.6 \times 10^9$ (Pa)
$c_{r\theta}^{(a)} = 74.3 \times 10^9$ (Pa)	$c_{r\theta}^{(b)} = 39.3 \times 10^9$ (Pa)
$c_{\theta\varphi}^{(a)} = 77.8 \times 10^9$ (Pa)	$c_{\theta\varphi}^{(b)} = 45.2 \times 10^9$ (Pa)
$c_{\theta\theta}^{(a)} = 139 \times 10^9$ (Pa)	$c_{\theta\theta}^{(b)} = 74.1 \times 10^9$ (Pa)
$e_{rr}^{(a)} = 15.1$ (Cm^{-2})	$e_{rr}^{(b)} = 0.347$ (Cm^{-2})
$e_{r\theta}^{(a)} = -5.2$ (Cm^{-2})	$e_{r\theta}^{(b)} = 0.16$ (Cm^{-2})
$\varepsilon_{rr}^{(a)}$ $= 3.87 \times 10^{-9}$ (C^{2}K^{-1}m^2)	$\varepsilon_{rr}^{(b)}$ $= 9.03 \times 10^{-11}$ (C^{2}K^{-1}m^2)
$p_{11}^{(a)}$ $= -2.5 \times 10^{-5}$ (CK^{-1}m^{-2})	$p_{11}^{(b)}$ $= -2.94 \times 10^{-6}$ (CK^{-1}m^{-2})
$\alpha_r^{(a)} = 2 \times 10^{-5}$ (K^{-1})	$\alpha_r^{(b)} = 2.458 \times 10^{-6}$ (K^{-1})
$\alpha_\theta^{(a)} = 2 \times 10^{-6}$ (K^{-1})	$\alpha_\theta^{(b)} = 4.396 \times 10^{-6}$ (K^{-1})
$\eta_r^{(a)}$ $= 0.03 \times c_{rr}^{(a)}$ (m^{3}kg^{-1}Pa)	$\eta_r^{(b)} = 0.03 \times c_{rr}^{(b)}$ (m^{3}kg^{-1}Pa)
$\eta_\theta^{(a)} = 0$ (m^{3}kg^{-1}Pa)	$\eta_\theta^{(b)} = 0$ (m^{3}kg^{-1}Pa)
$\mu^{(a)} = 4\pi \times 10^{-7}$(Hm^{-1})	$\mu^{(b)} = 6.15 \times 10^{-5}$(Hm^{-1})

The effective material properties of FGP structures with porosity are expressed as a power function of radius $P(r)$ in the form

$$P(r) = \left(p^{(b)} - p^{(a)}\right)\left(\frac{r-a}{b-a}\right)^l + p^{(a)} - \frac{\beta}{2}\left(p^{(a)} + p^{(b)}\right), \tag{1}$$

where p_a and p_b are the properties of internal and external surfaces; a and b are the inner and outer radius, respectively; $l \geq 0$ is the volume fraction exponent (l is a grading index), and $0 \leq \beta \leq 1$ is a porosity volume parameter, for non-porous shape $\beta = 0$.

The porous hollow structures loading is a collection of moisture diffusion $C(r)$, temperature conduction $T(r)$ and electric potential $\psi(r)$ placed in a stable magnetic field. The constitutive equations for the porous FGP structures in the radial direction are expressed as (Sinha, 1962; Dai and Wang, 2005):

$$\begin{Bmatrix}\sigma_r \\ \sigma_\theta\end{Bmatrix} = \begin{bmatrix}c_{rr} & nc_{r\theta} & e_{rr} \\ c_{r\theta} & c_n & e_{r\theta}\end{bmatrix}\begin{Bmatrix}\frac{du}{dr} \\ \frac{u}{r} \\ \frac{d\psi}{dr}\end{Bmatrix} - $$

$$\begin{Bmatrix}\lambda_r \\ \lambda_\theta\end{Bmatrix}T(r) - \begin{Bmatrix}\eta_r \\ \eta_\theta\end{Bmatrix}C(r), \tag{2}$$

$$D_r = e_{rr}\frac{du}{dr} + ne_{r\theta}\frac{u}{r} - \varepsilon_{rr}\frac{d\psi}{dr} + p_{11}T(r) + p_{22}C(r), \tag{3}$$

where n is a unified parameter, $n = 1$ for cylindrical coordinates, and $n = 2$ for spherical coordinates, respectively. Also, $c_1 = c_{\theta\theta}$ and $c_2 = c_{\theta\theta} + c_{\theta\varphi}$. Furthermore, c_{ij} ($i, j = r, \theta, z$)

for cylinder, c_{ij} ($i, j = r, \theta, \varphi$) for sphere, $e_{r\theta}$ ($j = r, \theta$), ε_{rr}, p_{11}, p_{22} and η_i ($i = r, \theta$) are elastic, piezoelectric, dielectric, pyroelectric, hygroelectric and moisture expansion constants, while λ_i related to the material coefficients in the forms

$$\begin{Bmatrix}\lambda_r \\ \lambda_\theta\end{Bmatrix} = \begin{bmatrix}c_{rr} & nc_{r\theta} \\ c_{r\theta} & c_n\end{bmatrix}\begin{Bmatrix}\alpha_r \\ \alpha_\theta\end{Bmatrix}, \tag{4}$$

where α_i are the thermal expansion coefficients. Consider the magnetic permeability $\mu(r)$ of porous FGP hollow structures are the same as the magnetic permeability of its medium (Ezzat, 1997). The characteristic properties of the medium are non-ferromagnetic and non-ferroelectric neglecting the Thompson effect. Maxwell's equations of electrodynamics written (Kraus, 1984)

$$\left.\begin{aligned}\underline{J} = \nabla \times \underline{h}, \qquad \nabla \times \underline{e} = -\mu\frac{\partial \underline{h}}{\partial t}, \\ \nabla \cdot \underline{h} = 0, \qquad \underline{e} = -\mu\left(\frac{\partial u}{\partial t} \times \underline{H}\right), \\ \underline{h} = \nabla \times \left(\underline{u} \times \underline{H}\right)\end{aligned}\right\} \tag{5}$$

The vector of the initial magnetic $\underline{H} \equiv (0,0,H)$ and displacement field $\underline{u} \equiv (u,0,0)$ while $\underline{h} \equiv (0,0,h)$, substitute in Eq. (5)

$$\left.\begin{aligned}\underline{e} = -\mu(r)\left(0, H\frac{\partial u}{\partial t}, 0\right) \\ \underline{J} = \left(0, -\frac{\partial h}{\partial r}, 0\right) \\ h = -H\left(\frac{\partial u}{\partial r} + \frac{2u}{r}\right)\end{aligned}\right\} \tag{6}$$

where H in Eq. (6) represent H_z in cylindrical coordinates and H_φ in spherical coordinates. As a rule, suppose that c_{ij}^n, e_{rj}, α_i, η_i, μ, p_{11} and p_{22} of the porous structures tracking power graded function in Eq. (1).

Uncoupled hygrothermal distribution

The uncoupled equations of temperature and moisture are independent. Fourier heat equation and Fickian moisture diffusion along the radial direction can be written in the form (Kraus, 1984; Sih *et al.*, 1986):

$$\left.\begin{aligned}\frac{1}{r^n}\frac{d}{dr}\left(k_T r^n \frac{dT(r)}{dr}\right) = 0, \\ \frac{1}{r^n}\frac{d}{dr}\left(k_C r^n \frac{dC(r)}{dr}\right) = 0,\end{aligned}\right\} \tag{7}$$

where k_T, k_C is the mean of heat conductivity constant and the mean of moisture diffusivity constant, respectively.

The boundary conditions for temperature and moisture in both cylindrical and spherical coordinates are expressed as

$$T^{(n)}(r)\big|_{r=a} = T_0, \qquad T^{(n)}(r)\big|_{r=b} = T_1,$$
$$C^{(n)}(r)\big|_{r=a} = 0, \qquad C^{(n)}(r)\big|_{r=b} = C_0,$$
(8)

where T_0 is reference primary temperature, C_0 is the primary moisture concentration and T_1 is the value of temperature at $r = b$.

By integrating Eqs. (7) twice and applying the boundary conditions (8), one can solve the equations as

$$T^{(1)}(r) = T_0 + \frac{T_1 - T_0}{\ln\left(\frac{b}{a}\right)} \ln\left(\frac{r}{a}\right),$$

$$C^{(1)}(r) = C_0 \frac{\ln\left(\frac{r}{a}\right)}{\ln\left(\frac{b}{a}\right)} \ln\left(\frac{r}{a}\right),$$
(9)

$$T^{(2)}(r) = \frac{bT_0}{b-a}\left[\frac{T_1}{T_0} - \frac{a}{b} + \frac{a}{r}\left(1 - \frac{T_1}{T_0}\right)\right],$$

$$C^{(2)}(r) = \frac{bC_0}{b-a}\left(1 - \frac{a}{r}\right).$$

Equilibrium and Maxwell equations

The equilibrium and electric displacement (Maxwell) equations of FGP porous hollow structures in one dimension by ignoring electric charge density and body force are (Paria, 1967):

$$\frac{d\sigma_r}{dr} + \frac{n(\sigma_r - \sigma_\theta)}{r} + F = 0, \tag{10}$$

$$\frac{dD_r}{dr} + \frac{nD_r}{r} = 0, \tag{11}$$

where F represents Lorentz force. It can express as

$$\frac{d^2u}{dr^2} + \left(\frac{\frac{dm_{11}}{dr} + H^2\frac{d\mu}{dr}}{m_{11} + \mu H^2} + \frac{n}{r}\right)\frac{du}{dr} + n\left(\frac{\frac{dm_{12}}{dr} + H^2\frac{d\mu}{dr}}{r(m_{11} + \mu H^2)} + \frac{(n-1)m_{12} - m_{22} - \mu H^2}{r^2(m_{11} + \mu H^2)}\right)u + \frac{m_{41}}{m_{11} + \mu H^2}\frac{dC}{dr} + \left(\frac{\frac{dm_{41}}{dr}}{m_{11} + \mu H^2} + \right.$$

$$\left. \frac{n(m_{41} - m_{42})}{r(m_{11} + \mu H^2)}\right)C(r) + \frac{m_{31}}{m_{11} + \mu H^2}\frac{dT}{dr} + \left(\frac{\frac{dm_{31}}{dr}}{m_{11} + \mu H^2} + \frac{n(m_{31} - m_{32})}{r(m_{11} + \mu H^2)}\right)T(r) - \left(\frac{\frac{dm_{51}}{dr}}{r^n(m_{11} + \mu H^2)} - \right.$$

$$\left. \frac{nm_{52}}{r^{n+1}(m_{11} + \mu H^2)}\right)A_1 = 0, \tag{15}$$

where m_{ij} are functions of r

$$m_{11} = c_{rr} + \frac{e_{rr}^2}{\varepsilon_{rr}}, \qquad m_{12} = c_{r\theta} + \frac{e_{rr}e_{r\theta}}{\varepsilon_{rr}},$$
$$m_{22} = c_n + n\frac{e_{r\theta}^2}{\varepsilon_{rr}}, \qquad m_{31} = \frac{e_{rr}p_{11}}{\varepsilon_{rr}} - \lambda_r,$$
$$m_{32} = \frac{e_{r\theta}p_{11}}{\varepsilon_{rr}} - \lambda_\theta, \qquad m_{41} = \frac{e_{rr}p_{22}}{\varepsilon_{rr}} - \eta_r,$$
$$m_{42} = \frac{e_{r\theta}p_{22}}{\varepsilon_{rr}} - \eta_\theta, \qquad m_{51} = \frac{e_{rr}}{\varepsilon_{rr}},$$
$$m_{52} = \frac{e_{r\theta}}{\varepsilon_{rr}},$$
(16)

To complete the solution of the problem after getting the general solution of radial displacement in Eq. (15), substitute in Eq. (14) and integrate with an additional constant of integration A_2 to obtain the electric potential $\psi(r)$.

$$F = \mu(r)\left(\underline{J} \times \underline{H}\right) = H^2 \frac{\partial}{\partial r}\left(\mu\frac{du}{dr} + \mu\frac{nu}{r}\right). \tag{12}$$

Elastic solution procedure for the porous structures

The solution technique for porous FGP hollow structures is obtained by solving the uncoupled equations for temperature and moisture first, the next step solves the equilibrium and electric displacement equations with mechanical and electric conditions.

Temperature distribution and moisture concentration equations are having been shown in Eqs. (9), and the electrostatic charge solution in Eq. (11) is expressed in the form

$$D_r = \frac{A_1}{r^n}, \tag{13}$$

where A_1 is constant of integration. Then, Eqs. (3) and (13) with a graded power function in Eq. (1), yields

$$\frac{d\psi}{dr} = \frac{1}{\varepsilon_{rr}}\left(e_{rr}\frac{du}{dr} + ne_{r\theta}\frac{u}{r} + p_{11}T(r) + p_{22}C(r) - \frac{A_1}{r^n}\right). \tag{14}$$

By substituting in equilibrium equation Eq. (10) and collecting the terms of radial displacement derivatives in a different order, temperature and moisture can be summarized as

Now, the boundary conditions on the porous hollow structures are divided into mechanical and electric boundary conditions

Mechanical boundary conditions
$$\sigma_r|_{r=a} = -P_1, \quad \sigma_r|_{r=b} = -P_2.$$

Electric boundary conditions
$$\psi(r)|_{r=a} = \psi_1, \quad \psi(r)|_{r=b} = \psi_2.$$

where P_1, P_2 are the pressures on internal and external radii and ψ_1, ψ_2 are the value of electric potentials on the inner and outer radius.

To finish the solution of Eq. (15) as a function of r is too difficult. So, it is suitable to employ a semi-analytical technique to obtain the solution of the differential equation (15). In this technique, the radial range is split into some virtual sub-domains with a thickness $s^{(k)}$, as

presented in Fig. 1. Evaluating the factors of Eq. (15) at $r = r^{(k)}$, the mean radius of the kth division, and using them as suitable variable coefficients in Eq. (15), that is

$$N_1^{(k)} = \left.\frac{\frac{dm_{11}}{dr} + H^2\frac{d\mu}{dr}}{m_{11} + \mu H^2}\right|_{r=r^{(k)}} + \frac{n}{r^{(k)}},$$

$$N_2^{(k)} = n\left(\left.\frac{\frac{dm_{12}}{dr} + H^2\frac{d\mu}{dr}}{r(m_{11} + \mu H^2)}\right|_{r=r^{(k)}} + \left.\frac{(n-1)m_{12} - m_{22} - \mu H^2}{r^2(m_{11} + \mu H^2)}\right|_{r=r^{(k)}}\right),$$

$$N_3^{(k)} = \left.\frac{m_{41}}{m_{11} + \mu H^2}\right|_{r=r^{(k)}}\left.\frac{dC}{dr}\right|_{r=r^{(k)}} + \left(\left.\frac{\frac{dm_{41}}{dr}}{m_{11} + \mu H^2}\right|_{r=r^{(k)}} + \left.\frac{n(m_{41} - m_{42})}{r(m_{11} + \mu H^2)}\right|_{r=r^{(k)}}\right)C(r^{(k)})$$

$$+ \left.\frac{m_{31}}{m_{11} + \mu H^2}\right|_{r=r^{(k)}}\left.\frac{dT}{dr}\right|_{r=r^{(k)}} + \left(\left.\frac{\frac{dm_{31}}{dr}}{m_{11} + \mu H^2}\right|_{r=r^{(k)}} + \left.\frac{n(m_{31} - m_{32})}{r(m_{11} + \mu H^2)}\right|_{r=r^{(k)}}\right)T(r^{(k)})$$

$$- \left(\left.\frac{\frac{dm_{51}}{dr}}{r^n(m_{11} + \mu H^2)}\right|_{r=r^{(k)}} - \left.\frac{nm_{52}}{r^{n+1}(m_{11} + \mu H^2)}\right|_{r=r^{(k)}}\right)A_1^{(k)},$$

while m_{ij} are functions of $r^{(k)}$. By using the up method, Eq. (15) with varying coefficients is changed into a set of m differential equations with constant coefficients and m is the number of virtual divisions. Now, we can acquire the displacement by solving Eq. (17) as a function of r in the form

$$u^{(k)} = B_1^{(k)}e^{\delta_1 r} + B_2^{(k)}e^{\delta_2 r} - \frac{N_3^{(k)}}{N_2^{(k)}}, \qquad (18)$$

where δ_1, δ_2 are the roots of the equation $\delta^2 + N_1^{(k)}\delta + N_2^{(k)} = 0$, and $B_1^{(k)}$ and $B_2^{(k)}$ are differential equation constants for kth division. The solution of Eq. (17) is valid for

$$r^{(k)} - \frac{s^{(k)}}{2} \le r \le r^{(k)} + \frac{s^{(k)}}{2},$$

where $r^{(k)}$ and $s^{(k)}$ are the mean radii and the radial thickness of the kth division, respectively. Constants $B_1^{(k)}$ and $B_2^{(k)}$ specified from the continuity boundary condition among every two neighboring divisions. So, the continuity boundary conditions are imposed at the interfaces of neighboring divisions in the form:

$$u^{(k)}\Big|_{r=r^{(k)}+\frac{S^{(k)}}{2}} = u^{(k+1)}\Big|_{r=r^{(k+1)}-\frac{S^{(k+1)}}{2}},$$

$$\sigma_r^{(k)}\Big|_{r=r^{(k)}+\frac{S^{(k)}}{2}} = \sigma_r^{(k+1)}\Big|_{r=r^{(k+1)}-\frac{S^{(k+1)}}{2}},$$

$$\sigma_\theta^{(k)}\Big|_{r=r^{(k)}+\frac{S^{(k)}}{2}} = \sigma_\theta^{(k+1)}\Big|_{r=r^{(k+1)}-\frac{S^{(k+1)}}{2}}, \qquad (19)$$

$$\psi^{(k)}\Big|_{r=r^{(k)}+\frac{S^{(k)}}{2}} = \psi^{(k+1)}\Big|_{r=r^{(k+1)}-\frac{S^{(k+1)}}{2}}.$$

By solving the continuity equations (19) with mechanical and electric boundary conditions together, one obtains a system of linear equations in $A_1^{(k)}$, $A_2^{(k)}$, $B_1^{(k)}$, $B_2^{(k)}$, ($k = 1,2,\dots,m$). Solving this system to determine

$$\frac{d^2u^{(k)}}{dr^2} + N_1^{(k)}\frac{du^{(k)}}{dr} + N_2^{(k)}u^{(k)} + N_3^{(k)} = 0, \qquad (17)$$

where

the constants and to get the radial displacement (18) in each subdomain. Rising the number of sub-domains improves the accuracy of the results.

Numerical examination

A numerical investigation is presented in Figs. 2-11 and Tables 2-9 to display the effect of porosity, moisture, temperature, and mechanical pressures on a porous piezoelectric functionally graded hollow structure (cylinder and sphere). The investigation is carried out for four different cases of boundary conditions for cylinder and sphere. In addition, suppose the inner and outer radius of porous structures are $a = 0.2$ (m) and $b = 1$ (m).
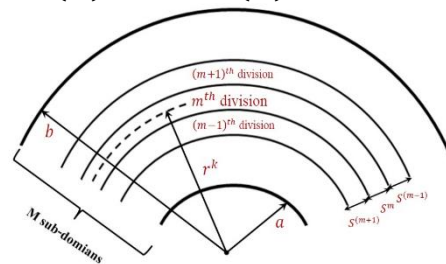

Figure 1. Dividing a radius range into several limited divisions.

All figures plotted for dimensionless rules:

$$\bar{r} = \frac{r}{b}, \qquad \bar{u} = \frac{u}{b} \times 10^2,$$

$$\bar{T} = \frac{T(\bar{r})}{T_0}, \qquad \bar{C} = \frac{C(\bar{r})}{C_0},$$

but, the dimensionless for stresses and electric potential will be changed for every case study. Consider PZT-4 and Cadmium selenide are the material of internal and external surfaces,

respectively. The value of the properties of the material is given in Table 1 (Ootao and Tanigawa, 2007; Ghorbanpour *et al.*, 2012).

The mechanical pressures and electric potentials boundary conditions are taken for a set of different formats in the following shape for a porous hollow (cylinder and sphere) sequentially:

Case 1:

$P_1 = 0$ (Pa), $P_2 = 0$ (Pa),

$\psi_1 = 0$ (W/A), $\psi_2 = 0$ (W/A).

Case 2:

$P_1 = 0$ (Pa), $P_2 = 10^{10}$ (Pa),

$\psi_1 = 0$ (W/A), $\psi_2 = 0$ (W/A).

Case 3:

$P_1 = 0$ (Pa), $P_2 = 0$ (Pa),

$\psi_1 = 10^8$ (W/A), $\psi_2 = 0$ (W/A),

Case 4:

$P_1 = 10^{10}$ (Pa), $P_2 = 0$ (Pa),

$\psi_1 = 0$ (W/A), $\psi_2 = 10^8 (W/A)$.

Numerical investigation for a porous hollow cylinder

Figure 2 shows the temperature and humidity according to Eq. (9) in the case of $n = 1$, which means the state of a porous hollow cylinder. Fig. (2a) describe the temperature behavior among the inner and outer surface of the cylinder. The temperature is equal to one at the inner surface compatible with the boundary condition and increasing along the radial direction. while Fig. (2b) presents the distribution of humidity as equal zero on the inner surface and equal one on the outer one to satisfy the boundary conditions.
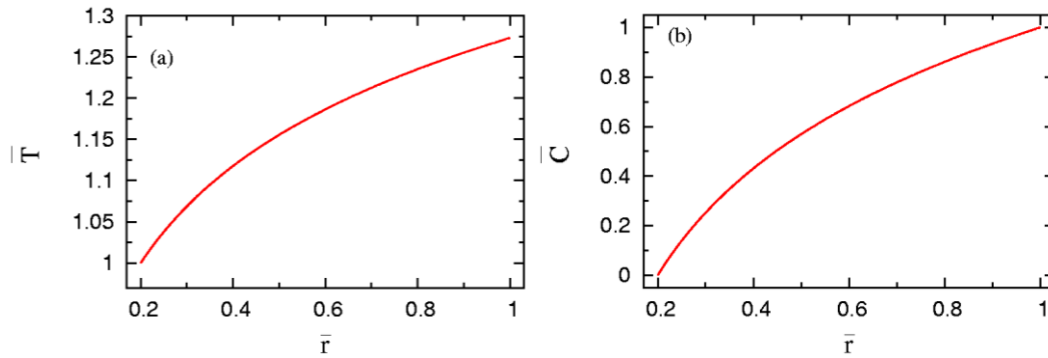

Figure 2. Temperature distribution and moisture condensation in FGP hollow cylinder.

Case 1: In this case, suppose that the mechanical pressures on the inner and outer surfaces equal zero and the cylinder is insulated. The dimensionless stresses and electric potential take the image:

$$\{\bar{\sigma}_r, \bar{\sigma}_\theta, \bar{\psi}\} = \{\sigma_r, \sigma_\theta, \psi\}.$$

Table 2 examines the difference between radial displacement, radial stress, hoop stress, and electric potential in perfect and porous FGP hollow cylinders with several values of grading index l. The table comparison between the perfect cylinder ($\beta = 0$) and porous cylinder ($\beta = 0.2$) with various values of grading index $l = 5, 10, 20$. The displacement values, radial stress, and electric potential amount in a porous cylinder are less than perfect values at the same dimensionless radius except for $l = 20$. The hoop stress is very sensitive to the porosity parameter β with different values of grading index l and dimensionless radius $\bar{r}$.

Figure 3 presents the case result. Radial and hoop stresses, electric potential, and radial displacement are shown in Fig. 3 with grading

index value $l = 12$ and different porosity factor values β. Figure 3(a) demonstrates the radial stress $\bar{\sigma}_r$ for various values of porosity factor ($\beta = 0, 0.1, 0.2, 0.3$). Noticed that, radial stress $\bar{\sigma}_r$ decreasing from $\bar{r} = 0.2$ to $\bar{r} = 0.3$ and then increasing to $\bar{r} = 0.9$ and thereafter decreasing close to the external surface $\bar{r} = 1$ to verify the boundary condition. Radial stress $\bar{\sigma}_r$ for a perfect cylinder $\beta = 0$ are intermediates of the porous cylinder along the radial direction. The hoop stress $\bar{\sigma}_\theta$ is displayed in Fig. 3(b) for a perfect and porous cylinder. The hoop stress $\bar{\sigma}_\theta$ are rising along the radius direction. Hoop stress $\bar{\sigma}_\theta$ for a perfect cylinder are intermediates the porous cylinder from $\bar{r} = 0.2$ to $\bar{r} = 0.65$ and then the perfect cylinder is greater than the identical ones of the porous cylinder. Figure 3(c) demonstrates the electric potential for the cylinder with various values of the parameter β. The electric potential is increasing along the cylinder radius and then decreases near the external surface to accept the boundary condition. The electric potential perfect curve is intermediating the porous curves for $\beta = 0.2$

and $\beta = 0.3$ along the radius direction. The radial displacement is explained in Figure 3(d). Displacement is increased over the radius of the

cylinder and the perfect curve is also amidst between $\beta = 0.2$ and $\beta = 0.3$ curves.
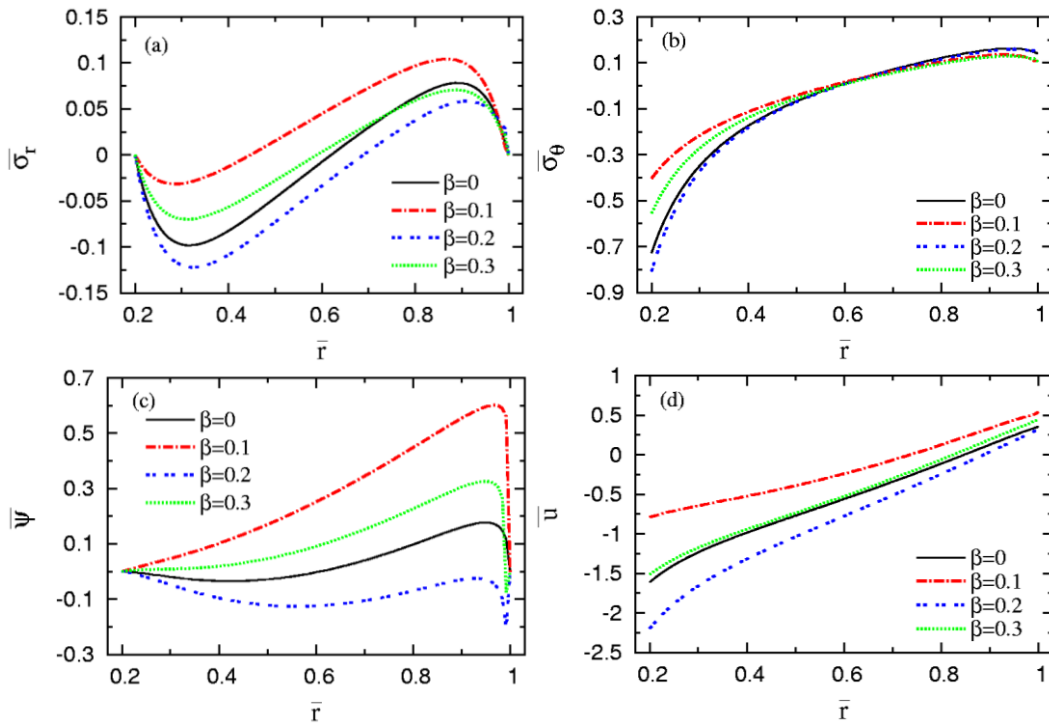

Figure 3. Influence of porosity parameter on stresses, electric potential, and displacement without mechanical loads and insulated FGP cylinder.

Case 2: For this case, there is only external pressure P_2 applied on the outer radius and there is no existence of electric potential on it. While the inner surface is free of mechanical and electrical loads. The cylinder in this case is

transacted as a sensor. The dimensionless has the form

$$\{\bar{\sigma}_r, \bar{\sigma}_\theta, \bar{\psi}\} = \left\{\frac{\sigma_r}{P_2}, \frac{\sigma_\theta}{P_2}, \psi\right\}.$$

Table 2. Influence of porosity parameter without mechanical loads and insulated the FGP cylinder.

	$\bar{r}$	Perfect FGPM ($\beta = 0$)			Porous FGPM ($\beta = 0.2$)		
		$l = 5$	$l = 10$	$l = 20$	$l = 5$	$l = 10$	$l = 20$
$\bar{u}$	0.3	-0.81709	-1. 1588	-1.4005	-1.1347	-1.4310	34.3381
	0.5	-0.47757	-0.71930	-0.88684	-0.66579	-0.89058	22.5822
	0.7	-0.11170	-0.30177	-0.43373	-0.21499	-0.40714	16.7232
$\bar{\sigma}_r$	0.3	-0.048208	-0.088570	-0.11643	-0.066632	-0.098795	3.2403
	0.5	0.00612	-0.03733	-0.06697	-0.01492	-0.05200	3.2764
	0.7	0.06551	0.03714	0.01322	0.04717	0.01974	2.5932
$\bar{\sigma}_\theta$	0.3	-0.24861	-0.33019	-0.38569	-0.26362	-0.33189	6.0008
	0.5	-0.032537	-0.061518	-0.079648	-0.031271	-0.061632	1.4176
	0.7	0.082183	0.073635	0.066493	0.082268	0.067483	0.18107
$\bar{\psi}$	0.3	0.01501	-0.013184	-0.03461	-0.011163	-0.026925	3.220
	0.5	0.08268	-0.00792	-0.07528	0.00163	-0.05701	10.087
	0.7	0.21165	0.07228	-0.03283	0.08710	-0.00514	15.779

The analysis of the case is shown in Table 3 and figure 4. Table 3 show the value of displacement, radial and hoop stresses, and electric potential for perfect and porous cylinder for the same value of radii and different value of grading index and porosity factor. It's clear that all value of displacement, stresses, and electric potentials in a perfect cylinder is greater than the value in a porous cylinder except the electric potential in a perfect cylinder is less

than the porous cylinder in the case of $l = 20$. Figure 4 shows the stresses, electric potential, and displacement in this case. Figure 4(a) illustrates the radial stress $\bar{\sigma}_r$ for a perfect and porous sensor cylinder. Radial stress decreases during the cylinder radius and satisfies the boundary condition. Notice that the perfect radial stress is less than the porous radial stress along the radius of the cylinder. While Figure 4(b) explains the hoop stress crosses the radial

direction. the hoop stress is increasing along the cylinder radius. Notice that the perfect radial stress is less than the porous radial stress along the radius of the cylinder. The same as radial stress, the perfect hoop stress is less than the porous hoop stress along the radius of the cylinder. The electric potential is drawn in Figure 4(c). it shows that the perfect electric potential is intermediating the porous curves along the radial coordinate. the electric potentials are increasing and then decreasing to

fulfill the boundary conditions. Figure 4(d) depicts the variation of displacement over the radius with different values of porosity factor β. The displacement is increasing for a plurality of cylinders and then decreases near the outer surface. The displacement perfect cylinder is intermediate to the porous ones from $\bar{r} = 0.2$ to $\bar{r} = 0.68$ and then the perfect cylinder is less than the corresponding ones.
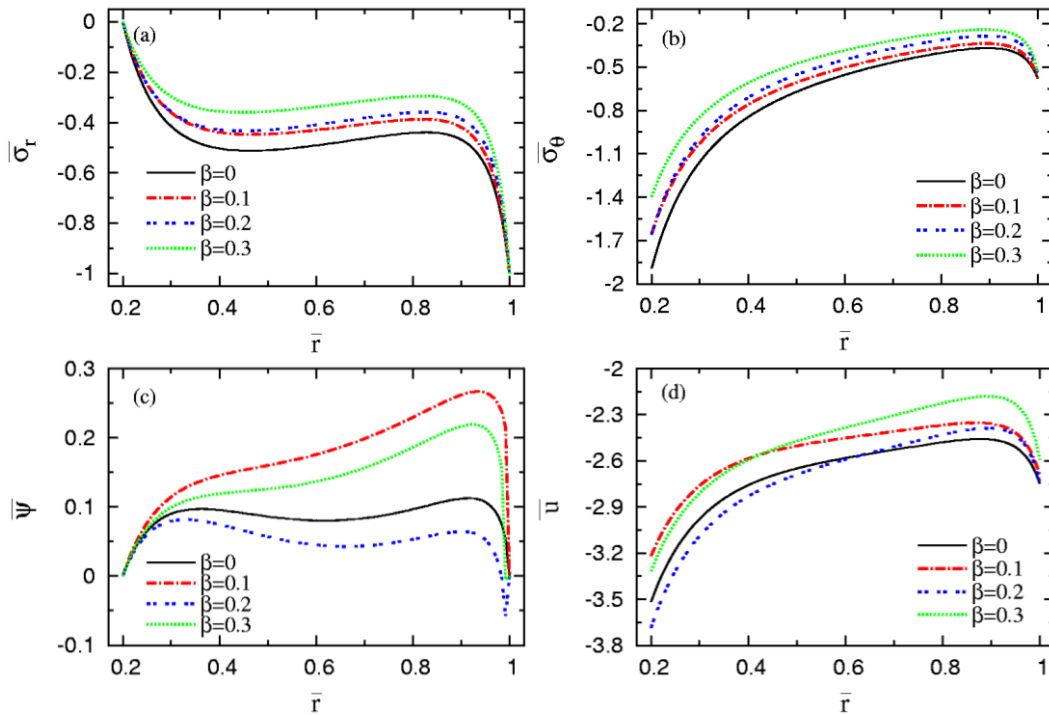

Figure 4. Influence of porosity parameter on stresses, electric potential, and displacement with mechanical loads and insulated FGP cylinder.

Table 3. Influence of porosity parameter with mechanical loads and insulated FGP cylinder.

	$\bar{r}$	Perfect FGPM ($\beta = 0$)			Porous FGPM ($\beta = 0.2$)		
		$l = 5$	$l = 10$	$l = 20$	$l = 5$	$l = 10$	$l = 20$
$\bar{u}$	0.3	-2.8749	-2.9462	-3.0603	-2.8453	-2.9860	12.6892
	0.5	-2.5772	-2.6284	-2.7065	-2.5199	-2.6422	7.66251
	0.7	-2.5029	-2.5130	-2.5717	-2.4114	-2.4604	5.04483
$\bar{\sigma}_r$	0.3	-0.40261	-0.41144	-0.42445	-0.33275	-0.34762	1.1152
	0.5	-0.49802	-0.50677	-0.52040	-0.40466	-0.42027	1.0378
	0.7	-0.47791	-0.46253	-0.47132	-0.38482	-0.37664	0.75215
$\bar{\sigma}_\theta$	0.3	-1.1298	-1.1484	-1.1740	-0.94047	-0.97151	1.8025
	0.5	-0.66258	-0.66945	-0.67737	-0.53846	-0.55045	0.096468
	0.7	-0.47792	-0.46739	-0.46914	-0.37949	-0.37265	-0.32326
$\bar{\psi}$	0.3	0.09788	0.09291	0.08245	0.09717	0.08879	1.5127
	0.5	0.11176	0.09483	0.06229	0.11670	0.08620	4.5335
	0.7	0.12291	0.09715	0.04660	0.13652	0.08897	7.0083

Case 3: The porous cylinder with purely electrical potential distribution on the inner surface and grounded on the external one. There is an absence of mechanical loading on the porous sphere. The cylinder in this status is like an actuator. The dimensionless take the image:

$$\{\bar{\sigma}_r, \bar{\sigma}_\theta, \bar{\psi}\} = \left\{\sigma_r, \sigma_\theta, \frac{\psi}{\psi_1}\right\}.$$

The product of this case is recorded in Table 4 and Figure 5. Table 4 clarify the value of displacement, stresses, and electric potential on an actuator porous cylinder for the various value

of porosity parameter β and grading index l. It's sharp from the table data that the value at $l = 5$ and $l = 10$ in a perfect cylinder for stresses, radial displacement, and electric potential is greater than the values of a porous cylinder with different porosity factors β. But, in the case of $l = 20$ the value of porous cylinder for displacement, stresses, and electric potential is the biggest ever.

The illustration of this case is shown in Figure 5. The radial stress appears in Figure 5(a), we note from them that the radial stress is decreasing from $\bar{r} = 0.2$ to $\bar{r} = 0.32$ and then increasing to verify the mechanical boundary condition. The perfect radial stress is amidst the porous cylinder curves. Figure 5(b) present the hoop stress along the radial direction on the cylinder. the hoop stress is growing through the radii of the cylinder. The perfect hoop stress is amidst the porous cylinder from $\bar{r} = 0.2$ to $\bar{r} = 0.7$ and then the perfect cylinder curve is greater than the porous ones. The electric potential is plotted in Figure 5(c). The figure shows that the electric potential accepts the electric boundary conditions of the cylinder. The perfect electric potential curve is in the middle of the porous electric potential curves of the cylinder. Figure 5(d) presents radial displacement through the radii direction. Displacement is increasing during the radial direction. The largest and smallest values of curves are porous curves.
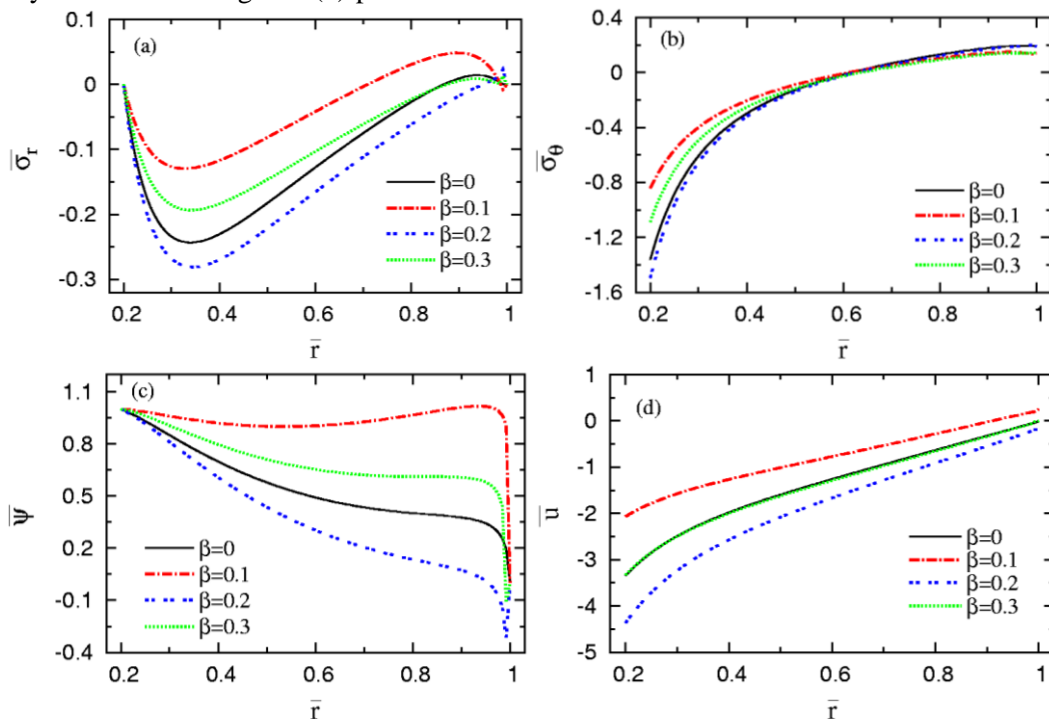

Figure 5. Influence of porosity parameter on stresses, electric potential, and displacement without mechanical loads and with electrical loads on FGP cylinder**.**

Table 4. Influence of porosity parameter without mechanical loads and with electrical loads on the FGP cylinder.

	$\bar{r}$	Perfect FGPM ($\beta = 0$)			Porous FGPM ($\beta = 0.2$)		
		$l = 5$	$l = 10$	$l = 20$	$l = 5$	$l = 10$	$l = 20$
$\bar{u}$	0.3	-1.8122	-2.3702	-2.7502	-2.4092	-2.8750	53.9792
	0.5	-1.1287	-1.5127	-1.7707	-1.5057	-1.8474	35.47022
	0.7	-0.58478	-0.87986	-1.0777	-0.83104	-1.1155	26.12623
$\bar{\sigma}_r$	0.3	-0.15634	-0.22034	-0.26326	-0.18608	-0.23488	5.0738
	0.5	-0.10081	-0.16857	-0.21316	-0.13377	-0.18926	5.1042
	0.7	-0.01202	-0.06360	-0.09962	-0.03911	-0.08708	4.0054
$\bar{\sigma}_\theta$	0.3	-0.45335	-0.57997	-0.66384	-0.49105	-0.59221	9.4770
	0.5	-0.079617	-0.11955	-0.14417	-0.085901	-0.12680	2.2292
	0.7	0.080403	0.069685	0.062023	0.077378	0.057503	0.24261
$\bar{\psi}$	0.3	0.91159	0.86122	0.82530	0.87435	0.84529	6.004
	0.5	0.77021	0.61256	0.50177	0.64296	0.54097	16.660
	0.7	0.72737	0.48793	0.31614	0.52399	0.36740	25.447

Case 4: Finally, the general case is a combination of mechanical and electrical

loading. In this study, the FGP cylinder effect by mechanical loading and grounded electric potential distribution on the internal surface but on the outer surface, there exist electric potential and is free of mechanical loading. Numerical outcomes are shown in Figure 6 and

tabulated in Table 5. The dimensionless stresses and electric potential distribution on the form:

$$\{\bar{\sigma}_r, \bar{\sigma}_\theta, \bar{\psi}\} = \left\{\frac{\sigma_r}{P_1}, \frac{\sigma_\theta}{P_1}, \frac{\psi}{\psi_2}\right\}.$$
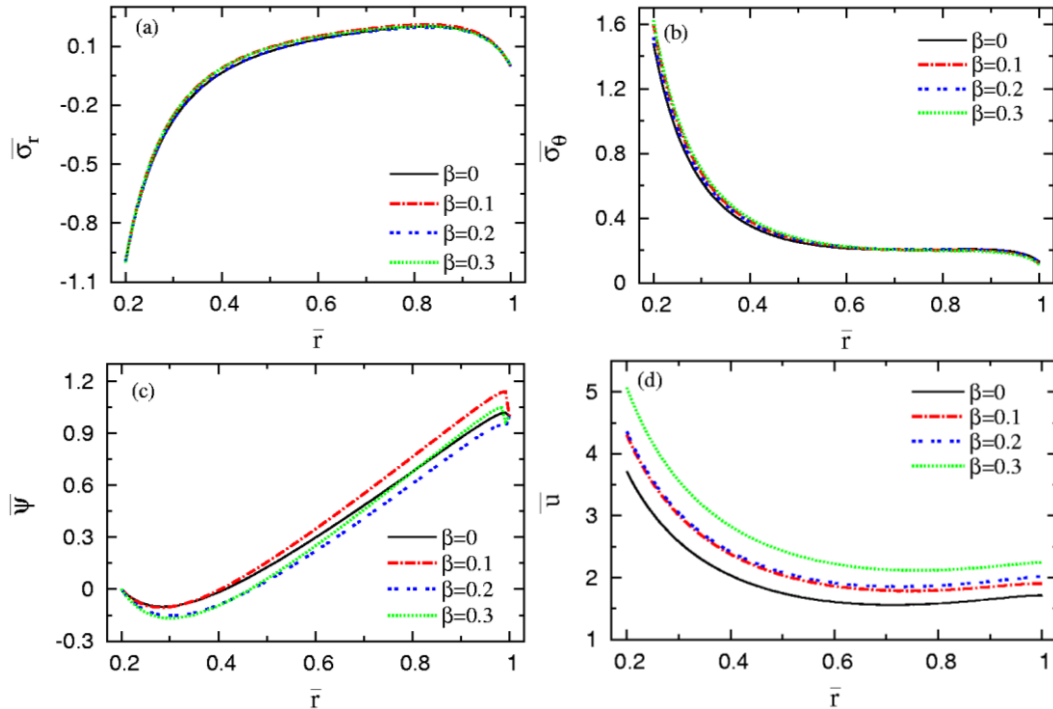

Figure 6. Influence of porosity parameter on stresses, electric potential, and displacement with mechanical and electrical loading on FGP cylinder.

Table 5. Influence of porosity parameter with mechanical and electrical loading on the FGP cylinder.

	$\bar{r}$	Perfect FGPM ($\beta = 0$)			Porous FGPM ($\beta = 0.2$)		
		$l = 5$	$l = 10$	$l = 20$	$l = 5$	$l = 10$	$l = 20$
$\bar{u}$	0.3	2.7568	2.6111	2.5191	3.2902	3.1258	12.98012
	0.5	1.8836	1.7694	1.6986	2.2689	2.1354	8.5907
	0.7	1.6787	1.5804	1.5177	2.0169	1.8956	6.5947
$\bar{\sigma}_r$	0.3	-0.25190	-0.27119	-0.28312	-0.24467	-0.26370	0.65428
	0.5	0.09788	0.07769	0.06389	0.10357	0.08310	0.99638
	0.7	0.17490	0.17767	0.16731	0.17517	0.17770	0.88445
$\bar{\sigma}_\theta$	0.3	0.67481	0.63318	0.60784	0.71090	0.66855	2.4074
	0.5	0.27485	0.25517	0.24338	0.29209	0.27056	0.67164
	0.7	0.21207	0.20610	0.19900	0.21782	0.20918	0.23444
$\bar{\psi}$	0.3	-0.08961	-0.09703	-0.10252	-0.14180	-0.14748	0.7511
	0.5	0.16025	0.13199	0.11249	0.09052	0.06597	2.8694
	0.7	0.53669	0.49350	0.46186	0.47678	0.43895	4.7991

In Table 5 the numerical data of radial displacement, radial and hoop stresses, and electric potential distribution in the porous cylinder are presented. The displacement and stresses for the perfect cylinder are less than those of the porous cylinder for all different values of grading index l and for several values of β. The perfect cylinder for electric potential is greater than the porous cylinder for electric potential on $l = 5$ and $l = 10$ but on $l = 20$ the porous electric potential values are the greatest.

Figure 6(a) indicates the radial stress along the dimensionless radius direction. The radial stress satisfies the boundary condition is equal to one on the inner surface and vanishes on the outer one. all radial stress curves with different porosity factor β coincide. Also, the hoop stress curves with various porosity factors β coincided, this is clear from figure 6(b). The hoop stress is decreased over the radius of the cylinder. Figure 6(c) demonstrates the electric potential. Figure 6(c) shows that the electric

potential is grounded on the inner surface and equal to one on the outer surface. The perfect electric potential curve is in the middle of the porous electric potential curves. Figure 6(d) clarify the radial displacement with different value of porosity factor β along the radius of the cylinder. The perfect displacement curve is the smallest one.

Numerical investigation for a porous sphere

Temperature distribution and moisture concentration in the case of porous spheres are shown in Figure 7 as stated by equation (9) for $n = 2$. Figure 7(a) presents the temperature on a porous sphere along the radius direction. The

temperature is increasing on the sphere radius. Also, the moisture curve describes monotonically increasing along the radii.

Case 1: The sphere mechanical loading is free and insulated. The dimensionless stresses and electric potential take the form:

$$\{\bar{\sigma}_r, \bar{\sigma}_\theta, \bar{\psi}\} = \{\sigma_r, \sigma_\theta, \psi\}.$$

Table 6 explains various locations of radial displacement, stresses, and electric potential in perfect and porous piezoelectric hollow spheres with different values of grading index and porosity parameter. All data in the table accepted that values in the perfect sphere are larger than the porous sphere values.
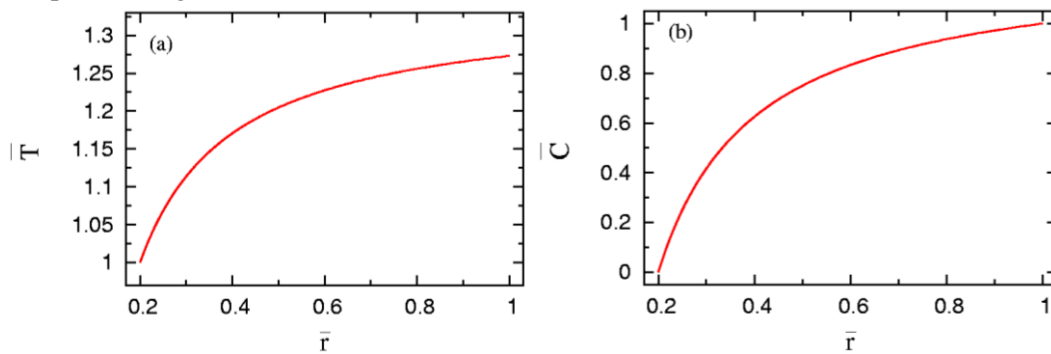

Figure 7. Temperature distribution and moisture condensation in FGP hollow sphere.

Figure 8 describes the effect of stresses, electric potential, and displacement on a hollow sphere with different values of porosity factor and for $l = 12$. It clarifies from Figure 8 that is almost like Figure 3 which illustrates the hollow cylinder. Figure 8(a) displayed the radial stress along the sphere radius. The radial stress also satisfies the boundary condition and the perfect sphere curve intermediates the porous sphere over the radial direction. The hoop stress is plotted in Figure 8(b). Notice that the hoop

stress is growing over the sphere radii. The perfect sphere curve firstly amidst the porous sphere curves and then the perfect sphere be the largest one. Figure 8(c) presents the electric potential of a hollow sphere through the radii. The electric potential is compatible with the grounded electric boundary condition. Figure 8(d) demonstrates the radial displacement of the sphere. The displacement is monotonically increasing along the radius direction. The perfect curve is intermediating the porous sphere curves.

Table 6. Influence of porosity parameter without mechanical loads and insulated the FGP sphere.

|	$\bar{r}$	Perfect FGPM ($\beta = 0$)			Porous FGPM ($\beta = 0.2$)		
		$l = 5$	$l = 10$	$l = 20$	$l = 5$	$l = 10$	$l = 20$
$\bar{u}$	0.3	-0.41008	-0.75826	-0.98747	-0.73852	-1.0054	-6.4463
	0.5	-0.16257	-0.33974	-0.45233	-0.29001	-0.4442	-2.8832
	0.7	0.14361	0.024557	-0.05191	0.10532	-0.01579	-1.4312
$\bar{\sigma}_r$	0.3	-0.090555	-0.17352	-0.22676	-0.13383	-0.19308	-1.2147
	0.5	-0.031054	-0.089722	-0.12637	-0.053910	-0.10147	-0.72737
	0.7	0.040523	0.012301	-0.010693	0.027975	0.000737	-0.34785
$\bar{\sigma}_\theta$	0.3	-0.24048	-0.32898	-0.38427	-0.26098	-0.32935	-1.3175
	0.5	-0.010511	-0.038681	-0.054181	-0.006821	-0.039151	-0.19168
	0.7	0.12604	0.11710	0.10916	0.12351	0.10749	0.09891
$\bar{\psi}$	0.3	0.07593	-0.0045289	-0.05941	0.001690	-0.04515	-1.2903
	0.5	0.22823	0.04708	-0.075882	0.06351	-0.48066	-2.8644
	0.7	0.38569	0.15601	-0.00244	0.17539	0.03443	-3.6068
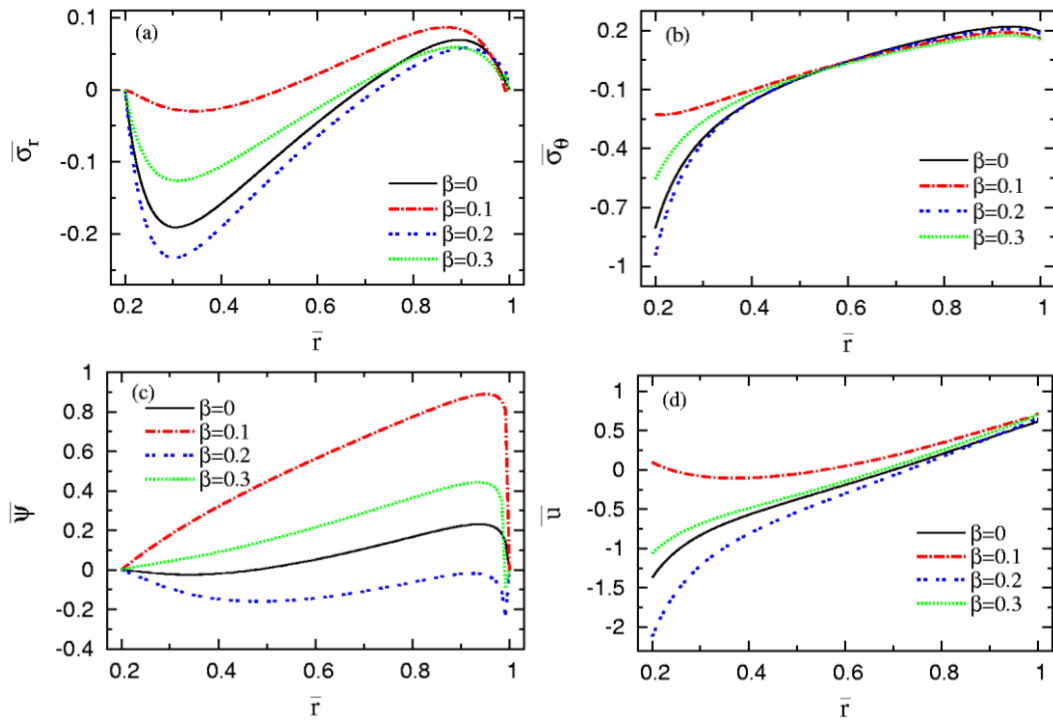
Figure 8. Influence of porosity parameter on stresses, electric potential, and displacement without mechanical loads and insulated FGP sphere.

Case 2: The sphere sensor is studied in this case with interior mechanical pressures only P_2, and grounded electric potential. Suppose dimensionless has style

$$\{\bar{\sigma}_r, \bar{\sigma}_\theta, \bar{\psi}\} = \left\{\frac{\sigma_r}{P_2}, \frac{\sigma_\theta}{P_2}, \psi\right\}.$$

The discussion of the sphere sensor is represented in Table 7 and Figure 9. Table 7

expounds on the variation in displacement, stresses, and electric potential for several values of porosity factor. For radial displacement and electric potential, Perfect sphere values are more major than the porous ones while all values of perfect radial and hoop stresses of the sphere are less than the porous sphere value except for $l = 20$.
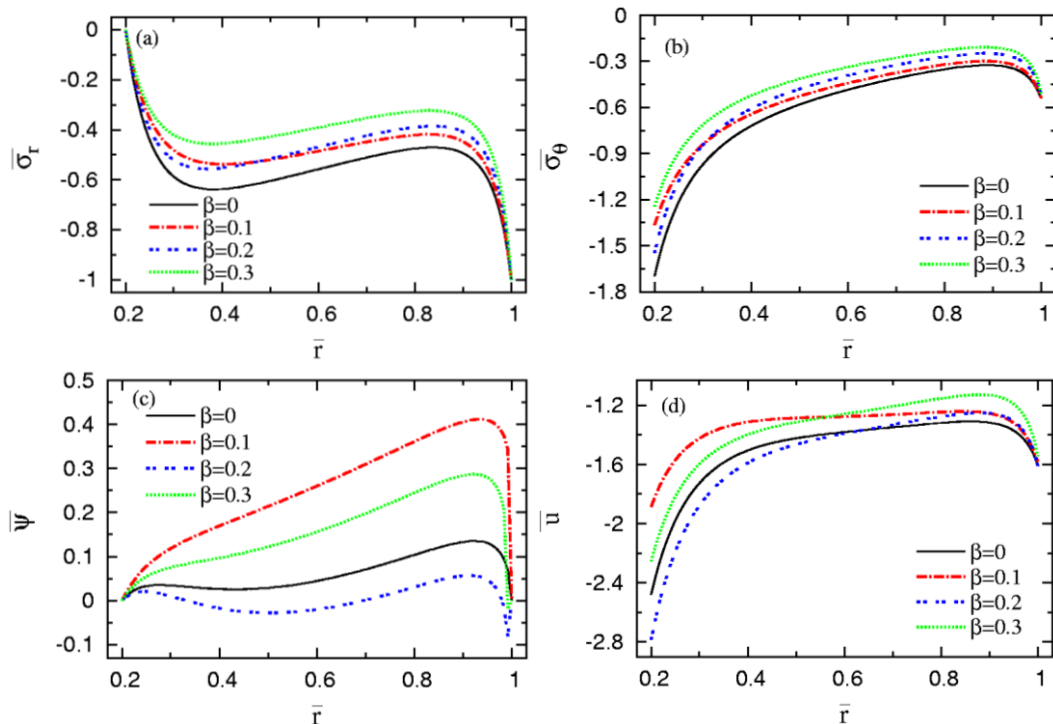

Figure 9. Influence of porosity parameter on stresses, electric potential, and displacement with mechanical loads and insulated FGP sphere.

Figure 9 demonstrates the radial stress, hoop stress, electric potential, and radial displacement in this case. Figure 9(a) shows the radial stress along the sphere radius. The radial stress increase while the porosity factor increases. The perfect radial stress of the sphere is the smallest one. Figure 9(b) explains the hoop stress along the radii. The hoop stress monotonically increases along the sphere radius. Also, the perfect hoop stress of the sphere is the smallest one. Electric potential is illustrated in Figure 9(c) with different porosity factors β. The electric potential satisfies the grounded boundary condition. Finally, Figure 9(d) presented the radial displacement with various porosity parameters. The displacement is monotonically increasing along the sphere radius. The perfect displacement sphere curve is between $\beta = 0.2$ and $\beta = 0.3$.

Table 7. Influence of porosity parameter with mechanical loads and insulated the FGP sphere.

	$\bar{r}$	Perfect FGPM ($\beta = 0$)			Porous FGPM ($\beta = 0.2$)		
		$l = 5$	$l = 10$	$l = 20$	$l = 5$	$l = 10$	$l = 20$
$\bar{u}$	0.3	-1.6015	-1.6953	-1.8024	-1.6397	-1.7749	-4.4244
	0.5	-1.3712	-1.4092	-1.4539	-1.3604	-1.4208	-2.6012
	0.7	-1.3574	-1.3433	-1.3635	-1.3111	-1.3100	-1.9847
$\bar{\sigma}_r$	0.3	-0.56150	-0.58134	-0.60379	-0.47661	-0.50247	-0.9982
	0.5	-0.59218	-0.60155	-0.61390	-0.49124	-0.50586	-0.80694
	0.7	-0.53459	-0.51154	-0.51443	-0.43841	-0.42084	-0.58415
$\bar{\sigma}_\theta$	0.3	-0.94701	-0.96550	-0.98596	-0.80127	-0.82684	-1.3038
	0.5	-0.58106	-0.58125	-0.58217	-0.47473	-0.47861	-0.59900
	0.7	-0.43117	-0.41132	-0.40744	-0.34255	-0.32646	-0.42463
$\bar{\psi}$	0.3	0.06813	0.042826	0.013637	0.06482	0.034707	-0.5748
	0.5	0.10248	0.04700	-0.01709	0.09637	0.02785	-1.3491
	0.7	0.16019	0.09382	0.01218	0.15538	0.07218	-1.7072

Case 3: In this case, the sphere actuator is shown without any mechanical loading and grounded outer surface, The electric potential on the internal surface of the sphere. The dimensionless can take the form:

$$\{\bar{\sigma}_r, \bar{\sigma}_\theta, \bar{\psi}\} = \left\{\sigma_r, \sigma_\theta, \frac{\psi}{\psi_1}\right\}.$$

The numerical outcomes are reported in Table 8 and Figure 10. Table 8 shows that values of displacement, stresses, and electric potential on the perfect functionally graded sphere are more major than the porous ones.

The discussion in Figure 10 is like the investigation in Figure 5. Figure 10(a) demonstrates the radial stress along the radial direction. The radial stress achieves the mechanical boundary condition. Figure 10(b) shows the hoop stress over the sphere radius. The hoop stress is growing over the radius direction. The perfect hoop stress curve is firstly in the middle of porous curves and then the perfect curve is the greatest one. The dimensionless electric potential is illustrated in Figure 10(c). The curves satisfy the grounded boundary condition on the outer surface and equal one on the inner one. The perfect electric potential curve is intermediate between the porous electric potential curves. Figure 10(d) presented the radial displacement over the sphere radii. The perfect displacement is amidst the porous displacement curves.

Table 8. Influence of porosity parameter without mechanical loads and with electrical loads on the FGP sphere.

|	$\bar{r}$	Perfect FGPM ($\beta = 0$)			Porous FGPM ($\beta = 0.2$)		
		$l = 5$	$l = 10$	$l = 20$	$l = 5$	$l = 10$	$l = 20$
$\bar{u}$	0.3	-1.3475	-1.8049	-2.0927	-1.8522	-2.1997	-8.9219
	0.5	-0.5831	-0.80835	-0.94666	-0.79325	-0.98451	-3.9937
	0.7	-0.10063	-0.24753	-0.33836	-0.19031	-0.33505	-2.0767
$\bar{\sigma}_r$	0.3	-0.29582	-0.40241	-0.46835	-0.34403	-0.41848	-1.6797
	0.5	-0.15657	-0.23021	-0.27436	-0.18318	-0.24130	-1.0125
	0.7	-0.02590	-0.06588	-0.09333	-0.04065	-0.078378	-0.50753
$\bar{\sigma}_\theta$	0.3	-0.43963	-0.55070	-0.61798	-0.46561	-0.56905	-1.7677
	0.5	-0.04230	-0.07364	-0.09067	-0.04095	-0.07436	-0.26257
	0.7	0.12457	0.11485	0.10706	0.12035	0.10229	0.09414
$\bar{\psi}$	0.3	0.83345	0.72435	0.65405	0.74841	0.68345	-0.8574
	0.5	0.69209	0.44787	0.29086	0.48986	0.33733	-3.1452
	0.7	0.69390	0.38652	0.18472	0.42927	0.23905	-4.2633
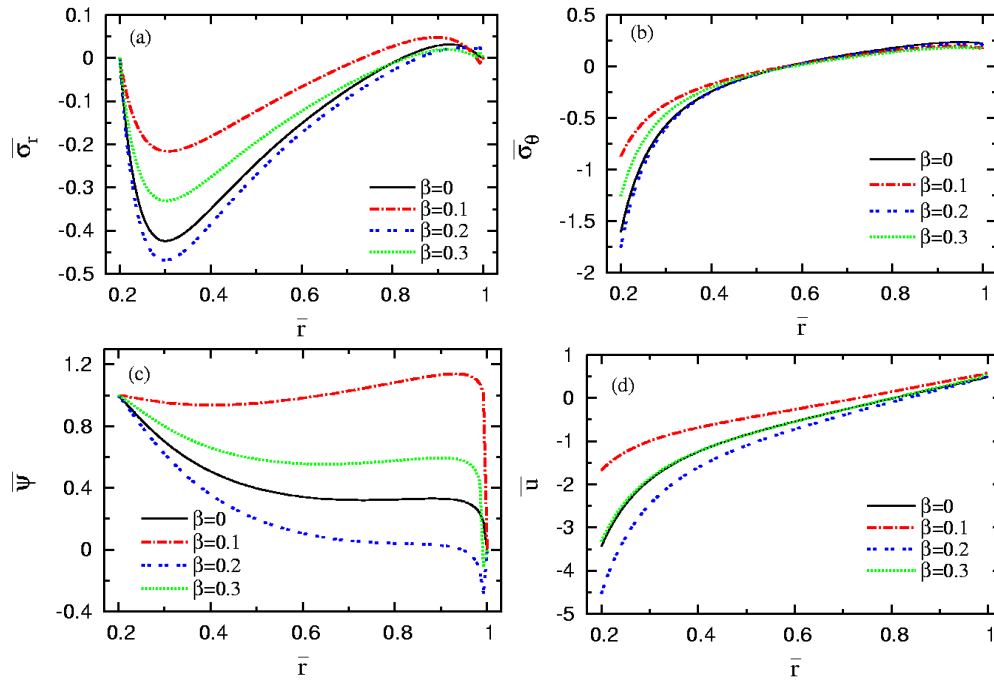
Figure 10. Influence of porosity parameter on stresses, electric potential, and displacement without mechanical loads and with electrical loads on FGP sphere.

Case 4: In case the force is a collection of mechanical pressure on the inner surface and electrical loading on the outer sphere surface. Numerical discussion is shown in Table 9 and Figure 11. Take the dimensionless in the form

$$\{\bar{\sigma}_r, \bar{\sigma}_\theta, \bar{\psi}\} = \left\{\frac{\sigma_r}{P_1}, \frac{\sigma_\theta}{P_1}, \frac{\psi}{\psi_2}\right\}.$$

Table 9 compares radial displacement, radial stress, hoop stress, and electrical potential for a sphere with various grading indexes l. Note that, all variables are very sensitive to the difference in the grading parameter l. The table explains that for the identical value of radii $\bar{r}$, the displacement and hoop stress the porous values are greater than the perfect values except for $l = 20$. but on the radial stress and electric potentials, the values of the porous sphere are minimum than the identical ones in the perfect sphere.

Figure 11(a) demonstrates the radial stress

along the sphere radius. The radial stress concurrent with the mechanical boundary condition is equal to one on the inner surface and vanishes on the outer one. Figure 11(b) shows the hoop stress curves with various porosity factors β. It clarifies that the hoop stress curves are similar in behavior, this is clear from Figure 11(b). The hoop stress is decreased along the radii of the cylinder. The perfect hoop stress curve is the smallest one. Figure 11(c) indicated the electric potential. Figure 11(c) shows that the electric potential satisfies the electric boundary condition. The perfect electric potential curve is intermediates to the porous electric potential curves. Figure 11(d) presents the radial displacement with the various values of porosity factor β along the radius of the sphere. The perfect displacement curve is the smallest one.

Table 9. Influence of porosity parameter with mechanical and electrical loading on the FGP sphere.

|	$\bar{r}$	Perfect FGPM ($\beta = 0$)			Porous FGPM ($\beta = 0.2$)		
		$l = 5$	$l = 10$	$l = 20$	$l = 5$	$l = 10$	$l = 20$
$\bar{u}$	0.3	1.3467	1.1236	0.96435	1.3946	1.2188	-2.5962
	0.5	0.60302	0.47956	0.39716	0.64659	0.53259	-1.1835
	0.7	0.59092	0.50200	0.44177	0.65788	0.56117	-0.44139
$\bar{\sigma}_r$	0.3	-0.0780	-0.13422	-0.17256	-0.10251	-0.14494	-0.86275
	0.5	0.09782	0.05603	0.028014	0.087418	0.05164	-0.39016
	0.7	0.12206	0.10909	0.091258	0.11635	0.10342	-0.14339
$\bar{\sigma}_\theta$	0.3	0.21134	0.14772	0.10644	0.21997	0.15761	-0.53873
	0.5	0.07707	0.05163	0.037502	0.086036	0.05819	-0.05414
	0.7	0.14817	0.13979	0.13123	0.14836	0.14443	0.12470
$\bar{\psi}$	0.3	0.1889	0.1420	0.1057	0.1051	0.0793	-0.7912
	0.5	0.6494	0.5416	0.4597	0.5115	0.4476	-1.5225
	0.7	1.0006	0.8620	0.75599	0.84530	0.7623	-1.7857
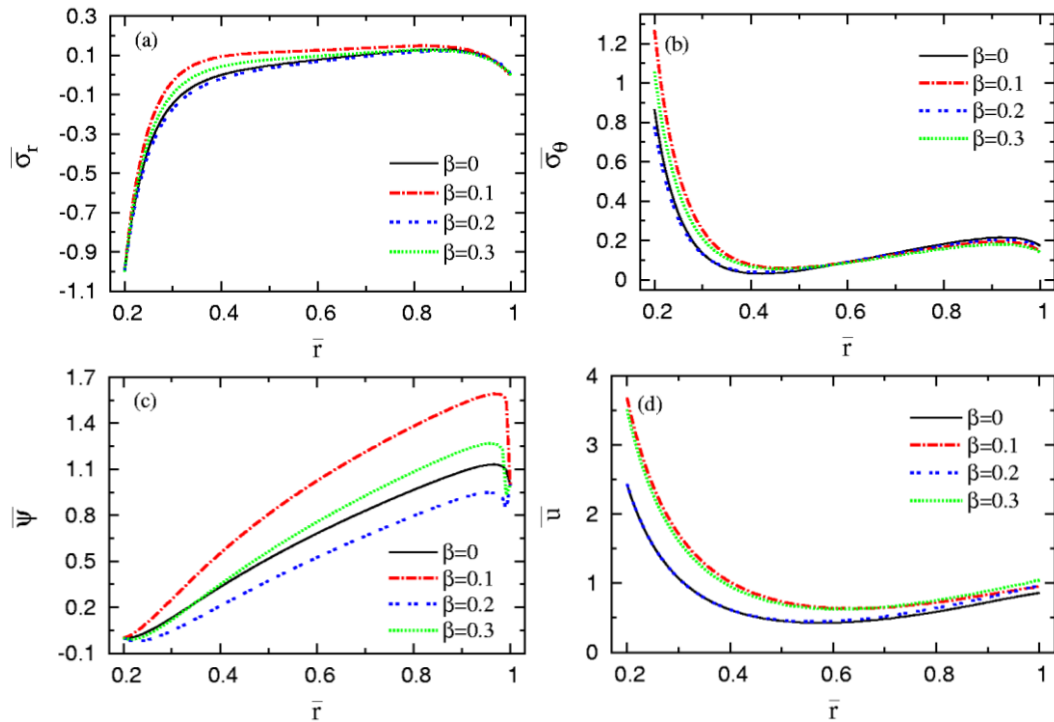
Figure 11. Influence of porosity parameter on stresses, electric potential, and displacement with mechanical and electrical loading on FGP sphere.

Conclusions

The survey discusses the influence of the porosity coefficient β under mechanical and electrical loading on a hygrothermal medium. Material characteristics of functionally graded piezoelectric hollow structures (cylinder and sphere) are indicated as a power radius function. Differential equations of equilibrium and Maxwell equations are solved by using the semi-analytical technique. The boundary conditions are discussed for a set of four different cases. During numerical outcomes and discussion there are some remarkable points as follows:

- The stresses, electric potential, and radial displacement are sensitive to the value of the porosity parameter.
- By choosing harmonious values for the porosity factor we gain specific values for stresses, displacement, and electric potential.
- the semi-analytical technique is active for obtaining particularly stressed value in perfect and porous structures.
- By comparing the results in the case of a porous hollow cylinder
  - The cylinder mechanical loading is free and insulated with different grading index, the stresses, radial displacement and electric potential values in a porous cylinder are less than perfect values at the same radius except for $l = 20$.
  - The cylinder with mechanical loading and grounded electric potential for several values of grading index, all values of stresses, displacement and electric potential in a porous cylinder are less than perfect values at the same radius except the electric potential in a perfect cylinder is less than porous cylinder for $l = 20$.
  - In the cylinder without mechanical loading and grounded outer surface with a different grading index, all values of stresses, displacement and electric potential in a porous cylinder are less than perfect values at the same radius except for $l = 20$ the values of stresses, displacement and electric potential in the porous cylinder is biggest ever.
  - The cylinder with mechanical and electrical loading, stresses and displacement for the perfect cylinder is less than those of the porous cylinder for all different values of the grading index. The electric potential values for the perfect cylinder are greater than the porous cylinder for $l = 5 \ and \ l = 10$

but on $l = 20$ the porous electric potential values are the greatest.

- By comparing the results in the case of a porous hollow sphere
  o In the sphere without mechanical loading and insulated with a different grading index, the stresses, radial displacement and electric potential values in a porous sphere are less than perfect values at the same radius.
  o The sphere with mechanical loading and insulated for several values of grading index, displacement and electric potential in a porous sphere are less than perfect ones while perfect values for radial and hoop stresses are less than the porous sphere except for $l = 20$.
  o In the sphere without mechanical loading and with internal electrical loads with different grading index, all values of stresses, displacement and electric potential in a porous sphere are less than perfect values at the same radius.

The sphere with mechanical and electrical loading, displacement and hoop stress for the porous sphere are greater than those of the perfect sphere, but the electric potential and radial stress values for the porous sphere are minimum than the perfect ones.

References

Ab Alghanmi RA, Zenkour AM (2021) Effect of porosity on the bending of functionally graded plates integrated with PFRC layer. *The European Physical Journal Plus* 136(2): 136-142, DOI: 10.1140/epjp/s13360-021-01123-6

Allam MNM, Tantawy R, Zenkour AM (2018) Magneto-thermo-elastic response of exponentially graded piezoelectric hollow spheres. *Advances in Computational Design* 3(3): 303-318, DOI: 10.12989/acd.2018.3.3.303

Allam MNM, Tantawy R, Zenkour AM (2016) Semi-empirical and efficient solutions for FGPM hollow spheres in hygrothermal environment. *KSCE Journal of Civil Engineering* 20(5): 1958–1965, DOI: 10.1007/s12205-015-0057-1

Arani AG, Kolahchi R, Barzoki AM, Loghman A (2012) Electro-thermo-mechanical behaviors of FGPM spheres using analytical method and ANSYS software. *Applied Mathematical Modelling* 36(1): 139-157, DOI: 10.1016/j.apm.2011.05.031

Arefi M, Zenkour AM (2017) Size-dependent

vibration and bending analyses of the piezomagnetic three-layer nanobeams. *Applied Physics A* 123: 202, DOI: 10.1007/s00339-017-0801-0

Dai HL, Jiang HJ, Yang L (2012) Time-dependent behaviors of a FGPM hollow sphere under the coupling of multi-fields. *Solid State Sciences* 14(5): 587-597, DOI: 10.1016/j.solidstatesciences.2012.02.011

Dai HL, Wang, X (2005) Thermo-electro-elastic transient responses in piezoelectric hollow structures. *International Journal of Solids and Structures* 42: 1151–1171, DOI: 10.1016/j.ijsolstr.2004.06.061

Ezzat MA (1997) Generation of generalized magnetothermoelastic waves by thermal shock in a perfectly conducting half-space. *journal of Thermal Stresses* 20: 633-917, DOI: 10.1080/01495739708956121

Fahsi B, Bouiadjra R Bachir, Mahmoudi A, Benyoucef S, Tounsi A (2019) Assessing the effects of porosity on the bending, buckling and vibrations of functionally graded beams resting on an elastic foundation by using a new refined quasi-3d theory. *Mechanics of Composite Materials* 55(2): 219-230, DOI: 10.1007/s11029-019-09805-0

Ghobadi Amin, Beni Yaghoub Tadi, Zur Krzysztof Kamil (2021) Porosity distribution effect on stress, electric field and nonlinear vibration of functionally graded nanostructures with direct and inverse flexoelectric phenomenon. *Composite Structures* 259: 113220, DOI: 10.1016/j.compstruct.2020.113220

Ghorbanpour Arani A, Kolahchi R, Mosallaie Barzoki AA, Loghman A (2021) Electro-thrmo-mechanical behaviors of FGPM spheres using analytical method and ANSYS software. *Applied Mathematical Modelling* 36: 139–157, DOI: 10.1016/j.apm.2011.05.031

Jankowski Piotr, Zur Krzysztof Kamil, Kim Jinseok, Lim CW, Reddy JN (2021) On the piezoelectric effect on stability of symmetric FGM porous nanobeams. *Composite Structures* 267: 113880, DOI: 10.1016/j.compstruct.2021.113880

Kraus JD (1984) Electromagnetic. *McGraw Hill, Inc., U.S.A.*

Nikrad SF, Kanellopoulos A, Bodaghi M, Chen ZT (2021) Large deformation behavior of functionally graded porous curved beams in thermal environment. *Archive of Applied Mechanics* 91: 2255–2278, DOI: 10.1007/s00419-021-01882-9

Ootao Y, Tanigawa Y (2007) Transient piezothermoelastic analysis for a functionally graded thermopiezoelectric hollow sphere. *Composite Structures* 81: 540–549, DOI: 10.1016/j.compstruct.2006.10.002

Paria G (1966) Magneto-elasticity and magneto-thermo-elasticity. *Advances of Applied Mechanics* 10(1): 73–112, DOI: 10.1016/S0065-2156(08)70394-6

Penna Rosa, Feo Luciano, Lovisi Giuseppe (2021) Hygro-thermal bending behavior of porous FG nano-beams via local/ nonlocal strain and stress gradient theories of elasticity. *Composite Structures* 263: 113627, DOI: 10.1016/j.compstruct.2021.113627

She GL, Ren YR, Yuan FG (2019) Hygro-thermal wave propagation in functionally graded double-layered nanotubes systems. *Steel and Composite Structures* 31(6): 641-653, DOI: 10.12989/scs.2019.31.6.641

Sih GC, Michopoulos JG, Chou SC (1986) Hygrothermoelasticity. *Dordrecht, Martinus Nijhoff Publisheres*

Singh SJ, Harsha SP (2021) Analysis of porosity effect on free vibration and buckling responses for sandwich sigmoid function based functionally graded material plate resting on Pasternak foundation using Galerkin Vlasov's method. *Journal of Sandwich Structures & Materials* 23(5): 1717–1760, DOI: 10.1177/1099636220904340

Sinha DK (1962) Note on the radial deformation of a piezoelectric polarized spherical shell with symmetrical temperature distribution. *Journal of the Acoustical Society of America* 34: 1073–1075, DOI: 10.1121/1.1918247

Sobhy M, Zenkour AM (2019) Porosity and inhomogeneity effects on the buckling and vibration of double-FGM nanoplates via a quasi-3D refined theory. *Composite Structures* 220: 289–303, DOI: 10.1016/j.compstruct.2019.03.096

Tahir Saeed I, Chikh Abdelbaki, Tounsi Abdelouahed, Al-Osta Mohammed A, Al-Dulaijan Salah U, Al-Zahrani Mesfer (2021)

Wave propagation analysis of a ceramic-metal functionally graded sandwich plate with different porosity distributions in a hygro-thermal environment. *Composite Structures* 269: 114030, DOI: 10.1016/j.compstruct.2021.114030

Tantawy R, Zenkour AM (2022) Effect of Porosity and Hygrothermal Environment on FGP Hollow Spheres under Electromechanical Loads. *Journal of Applied and Computational Mechanics* 8(2): 710–722, DOI: 10.22055/JACM.2021.39229.3377

Zenkour AM, Aljadani MH (2020) Buckling analysis of actuated functionally graded piezoelectric plates via a quasi-3D refined theory. *Mechanics of Materials* 151: 103632, DOI: 10.1016/j.mechmat.2020.103632

Zenkour AM, Alghanmi RA (2021) Hygro-thermo-electro-mechanical bending analysis of sandwich plates with FG core and piezoelectric faces. *Mechanics of Advanced Materials and Structures* 28(3): 282–294, DOI: 10.1080/15376494.2018.1562134

Zenkour AM, Alghanmi RA (2020) Static response of sandwich plates with FG core and piezoelectric faces under thermo-electro-mechanical loads and resting on elastic foundations. *Thin-Walled Structures* 157: 107025, DOI: 10.1016/j.tws.2020.107025

Zhang Y, Wang J (2017) Fabrication of functionally graded porous polymer structures using thermal bonding lamination techniques. *Procedia Manufacturing* 10: 866–875, DOI: 10.1016/j.promfg.2017.07.073

Zhao X, Zheng S, Li Z (2020) Effects of porosity and flexoelectricity on static bending and free vibration of AFG piezoelectric nanobeams. *Thin-Walled Structures* 151: 106754, DOI: 10.1016/j.tws.2020.106754.

<div dir="rtl">

الملخص العربي

عنوان البحث: التأثير الكهربي المغناطيسي على الهياكل المجوفة المصنوعة من مادة مسامية متدرجة الخواص في بيئة حرارية رطبة

رانيا محمد الطنطاوي*¹

¹ قسم الرياضيات، كلية العلوم، جامعة دمياط، مصر.

يعرض البحث تأثير المسامية والمجال المغناطيسي على نموذج رياضي لهياكل مجوفة مصنوعة من مادة متدرجة الخواص موصلة للكهرباء (FGP) (أسطوانة وكرة) في بيئة حرارية رطبة باستخدام طريقة الحل شبه التحليلي. يخضع النموذج الرياضي لتأثير العديد من القوى بالإضافة إلى المجال المغناطيسي الذي لا يزال يمثل دراسة صعبة. القوى المؤثرة عبارة عن ضغط ميكانيكي على السطح الداخلي والخارجي والمجال المغناطيسي والتأثير الحراري بالإضافة إلى تغير الجهد الكهربي بين السطح الداخلي والخارجي.

</div>

الدراسة افترضت أن جميع خصائص المادة متدرجة بواسطة دالة كثيرة حدود في نصف القطر. تناقش النتائج العددية أربعة شروط حدية مختلفة لكل نموذج موضحة الضغط الميكانيكي والمجال الكهربي الخاضع للتأثير الحراري والرطوبة والمجال المغناطيسي. للتحقق من النتائج العددية تم مقارنة النتائج بين الهياكل المجوفة المسامية وغير المسامية للمواد متدرجة الخواص. في نهاية الدراسة أوضحت النتائج العددية تأثير معامل المسامية في النماذج الرياضية وأهميته في الهندسة الميكانيكية والتكنولوجيا الحديثة.